Turkish Journal of Electrical Engineering & Computer Sciences

http://journals.tubitak.gov.tr/elektrik/

Research Article

Turk J Elec Eng & Comp Sci
(2014) 22: 1193 – 1209

doi:10.3906/elk-1203-29

Digital control system design and analyses of a 3-phase bearingless induction motor

Wenshao BU[1,*], Conglin ZU[1], Shaojie WANG[1], Shenghua HUANG[2]
[1]College of Information Engineering, Henan University of Science and Technology, Luoyang, P.R. China
[2]College of Electrical and Electronic Engineering, Huazhong University of Science and Technology, Wuhan, P.R. China

Received: 06.03.2012 • **Accepted:** 10.02.2013 • **Published Online:** 15.08.2014 • **Printed:** 12.09.2014

Abstract: The overall configuration of a magnetic suspension decoupling control system is designed to realize the reliable digital control of a 3-phase bearingless induction motor whose rotor windings are not pole-specific. Based on a digital signal processor complementary metal-oxide semiconductor chip, the digital control hardware and software systems are analyzed and designed. In this paper, the calculation and regulation of the motor rotational speed, correction and regulation methods of the radial displacements, calculation and compensation algorithms of the unilateral magnetic pulls, induction compensation algorithm of the effective suspension control current, current regulation, and space-vector pulse width modulation algorithms, are presented in detail. The experimental results verify the feasibility and practicability of the designed decoupling digital control system of the 3-phase bearingless induction motor.

Key words: Three-phase bearingless induction motor, magnetic suspension decoupling control, digital control system, measurement and regulation of signals, compensation and control

1. Introduction

A bearingless motor is proposed based on the comparability between the magnetic bearing and conventional motor stator in configurations. Compared to a motor with magnetic bearings, a bearingless motor has a series of advantages, such as shorter rotor shaft and higher critical speed. [1–5]. Presently, there exist urgent requirements for the control technology of a bearingless motor in some high-speed drive scopes, such as the high-speed drive of machine tool spindles, sealed transmission of material, and aviation and aerospace realms [1–4], making the bearingless motor a new research hotspot.

From the theory of the electromagnetic field, on the interface between 2 kinds of magnetic materials with different magnetic permeability, the Maxwell electromagnetism force will come into being. In bearingless motors, due to the magnetic permeability of the ferromagnetic material being much larger than that of air, the produced Maxwell forces are approximately vertical to their interface. If the air gap magnetic flux density is distributed symmetrically along the rotor surface, the resultant radial force is 0. The rotor's shift from the stator's center leads to the asymmetrical distributing of the air gap magnetic flux density. The air gap magnetic flux density in the area where the air gap decreases is enhanced; on the contrary, the air gap magnetic flux density in the area where the air gap increases is reduced. As a result, the resultant radial force will not equal

*Correspondence: wsbu@haust.edu.cn

0, and its direction will be in accordance with that of the rotor's shift [5,6]. The resultant radial force is called a unilateral magnetic pull.

To achieve stable suspension of the rotor, it is necessary to produce an additional radial force that can be controlled reliably. In a bearingless motor, an accessional set of suspension windings is embedded in the stator's slots, along with the conventional motor windings. When the current frequencies of 2 sets of windings, and their numbers of pole pairs, meet the qualifications in Eq. (1), a controllable resultant magnetic suspension radial force is produced [7–9].

$$p_2 = p_1 \pm 1, \omega_2 = \omega_1 \tag{1}$$

The controllable magnetic suspension force can be used to overcome the inner unilateral magnetic pulls and external radial load, and to achieve the stable suspension of the rotor [6]. That is the operation principle of the bearingless motor.

Bearingless technology can be used in almost all kinds of alternating current motors [1–9]. Recently, aiming at some kind of bearingless motor, research has been conducted on sensorless technology and unbalance vibration control technology [4,10,11]. The control system of the bearingless motor is an integrative automatization system, which integrates the theories and technologies of automation, motion control, power electronics, and computer control. The complicated control algorithms of the bearingless motor not only determine the characteristics of more calculation, but also determine the complexity of its decoupling control system [1,3,5,6]. It is gratifying that considerable development of microelectronic technology has been made. The widely used special integrated complementary metal-oxide semiconductor (CMOS) chip for motor control, i.e. digital signal processor (DSP) CMOS chip, has many merits, such as higher integration, higher ability of data processing, higher computing precision, abundant exterior ports, higher real-time performance, and lower price. Therefore, it provides convenience for achieving the decoupling digital control of a bearingless motor with higher performance.

There has been much research conducted regarding the control principle and model of a bearingless motor. However, the existing model and algorithm are basically based on a 2-phase bearingless motor [4–9]. At the same time, there are very few detailed reports in the literature about the design and implementation methods of the digital control system of the 3-phase bearingless motor.

Here, aiming at the 3-phase bearingless induction motor, the scheme of the decoupling control system, relevant models, and control algorithms are presented. After which, based on a single DSP CMOS chip, the implementation method of the decoupling digital control system is introduced, and the experimental results are presented.

2. Overall design of the magnetic suspension decoupling control system

Figure 1 shows the designed scheme of the decoupling digital control system of the 3-phase bearingless induction motor. In Figure 1, the reference signals of the radial displacement are compared with the corresponding measured signals, and using a proportional-integral-derivative (PID) regulator, the reference signals of the controllable magnetic suspension force, i.e. F_α^* and F_β^*, are derived. Next, by decoupling the algorithm, the signals of the suspension control current are derived. Here, to reduce the fabrication cost, the rotor windings of the 4-pole bearingless motor are not pole-specific, but the 2-pole suspension magnetic field inducts a current in the rotor windings, and then the suspension control current should be compensated for in the amplitude and phase.

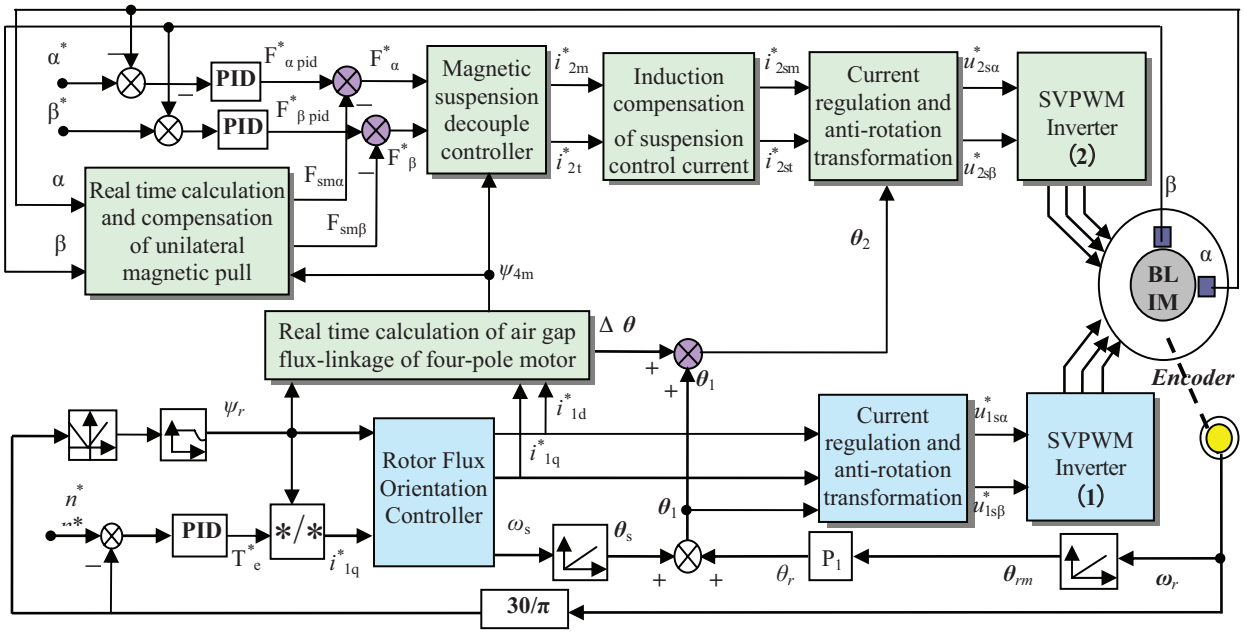

Figure 1. Scheme of the digital decoupling control system for the 3-phase bearingless induction motor.

In the decoupling calculation of the suspension control current, the phase angle of the 4-pole motor is required, and it is obtained using a real-time calculation. Moreover, to improve the stability of the suspension control system, the unilateral magnetic pulls are calculated and compensated online.

The decoupling control algorithm of the 3-phase bearingless induction motor is complicated, and its calculation workload is much greater than that of the conventional motor. To avoid a transferring delay of the information and to realize the decoupling control accurately, the TMS320LF2407A, a kind of special digital control CMOS chip applicable for the motor, is adopted to complete a dual function, i.e. not only acting as the controller of the 4-pole motor system, but also acting as that of a 2-pole magnetic suspension system. Relevant models and algorithms are introduced in the next section.

Figure 2 shows the hardware scheme of the decoupling digital control system of the 3-phase bearingless induction motor based on a single piece of DSP CMOS chip. In Figure 2:

1) The DSP controller is the core of the digital control system. It carries out all kinds of datum processing and control algorithms using software, such as the rotor flux orientation control of 4-pole motor, dynamic decoupling control and induction compensation of a 2-pole magnetic suspension system, regulation and calculation of all kinds of signals, and space-vector pulse width modulation (SVPWM).

The DSP CMOS chip will output 12 PWM signal routes, 6 of which are used to control the inverter of the 4-pole motor system, and the other 6 are used to control the inverter of the 2-pole magnetic suspension system.

2) The regulation and amplification circuit of the current. Using a Hall effect sensor, the measured armature current is converted into voltage signals. Before the analog-to-digital converter (ADC) conversion, the signals should be further processed, such as being adjusted at the electric level and being magnified in amplitude. Next, the signals should be within the range of 0 to 3.3 V.

3) The noncontact measurement, regulation, and amplification circuit of the radial displacements. After the measured radial displacements are converted into voltage signals by the whirlpool sensor, they are input

into the sampling circuit. By following the voltage, adjusting the levels, and amplifying the signals, the sampled signals are kept within the range of 0 to 3.3 V. Next, the sampled signals are sent to the ADC channels of the DSP CMOS chip.

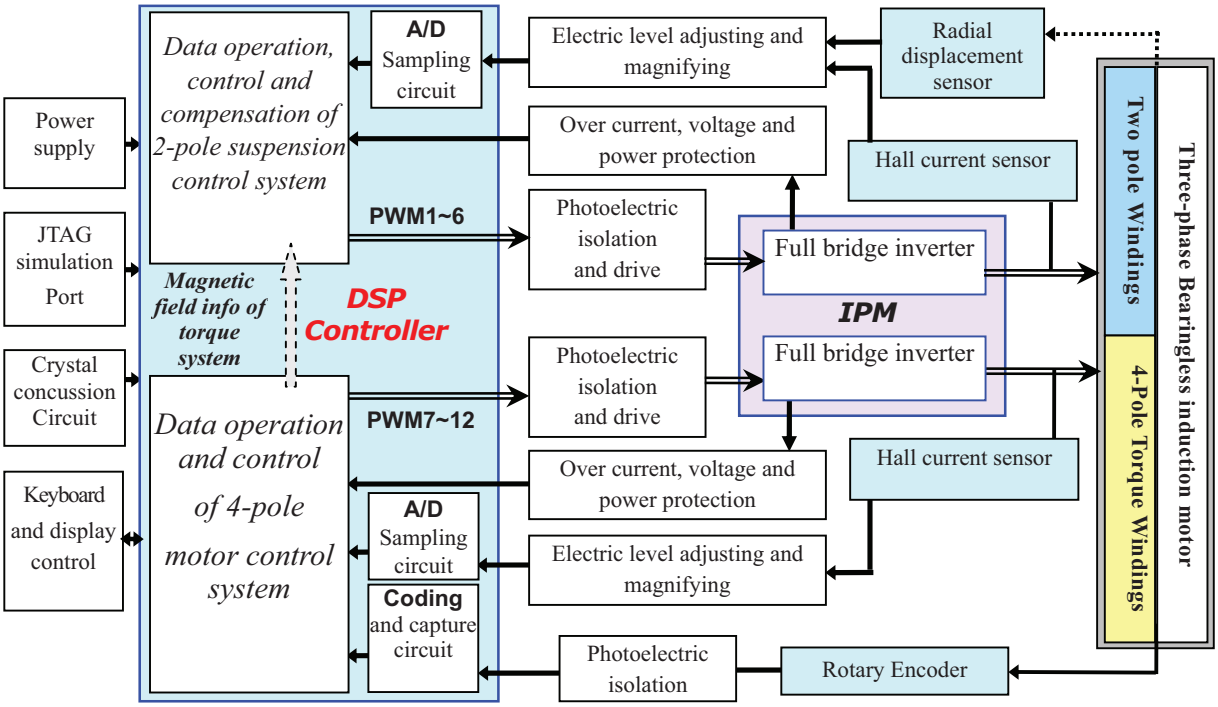

Figure 2. Digital control hardware scheme of the bearingless induction motor.

4) High speed photoelectric isolation and drive circuit. The SVPWM signals from the DSP are inputted into the photoelectric isolation circuit by the coupling resistance. The adopted photoelectric isolation circuit is designed based on the HCPL-0466, which is a kind of high-speed photoelectric coupling CMOS chip from the HP Corporation. The output signals from the photoelectric isolation circuit are filtered by the resistor-capacitor circuit, sent to the corresponding input ports of the IPM module FSBB20CH60, and control the switching state of the full bridge inverter that is integrated into the IPM module.

5) The keyboard and display circuit are designed based on the special digital CMOS chip of the ZLG7289A.

3. Software design and algorithm analyses of the decoupling digital control system

3.1. Software scheme of the digital control system

Figure 3 presents the main program flow chart of the decoupling digital control system of the 3-phase bearingless induction motor. The task of the main program is to accomplish the relevant initializations. More specifically, the tasks of the main program include following sections:

1) Input/output (I/O) port initialization of the DSP. By initialization, relevant I/O ports are set in input or output modes.

2) Initialization of the system timers. By initialization, the timing periods of T_1 and T_3 equal the period of the PWM signal, i.e. 0.1 ms, and the SVPWM modulation frequency is set as 10 kHz accordingly. The counter modes of T_1 and T_3 are set to continue adding and continue decreasing.

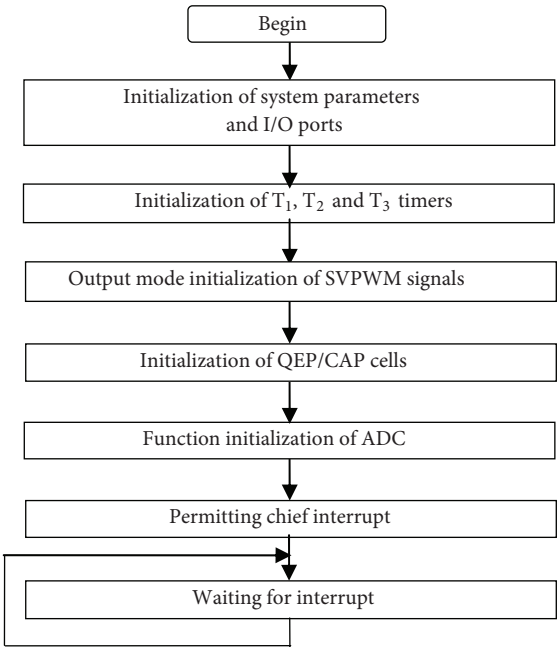

Figure 3. Main program flow chart of the decoupling digital control system.

3) Carrying out the measurement and calculation of the rotational speed, enabling the quadrature encoder pulse (QEP) counter function of the capturing cell in the DSP COMS chip, and setting T_2 as the counter of the QEP coding pulses.

4) Setting T_1 as the timing norm of the 3 comparing cells in event manager A (EVA), and setting T_3 as the timing norm of the 3 comparing cells in EVB. Two sets of comparing cells will be used to produce the SVPWM signals for the 4-pole motor system and 2-pole magnetic suspension system, respectively.

5) Initializing the ADC conversion compositor in rank-list mode, using the underflow occurrence of timer T_1 to start up the ADC conversion, using the ending occurrence of the ADC conversion to start up the ADC interrupt service program.

After all of the initializations, the interrupt response function of the system is opened and the system is in the state of waiting for interrupts, such as ADC and outer interrupts.

Aside from the initialization tasks, all kinds of numerical calculations, regulation algorithms, and SVPWM modulation functions are implemented in the ADC interrupt service program. More specifically, the main tasks of the ADC interrupt service program include: calculation and regulation of the rotational speed, flux orientation control of the 4-pole motor, vector transformation of the current and voltage, current regulation and SVPWM modulation, real-time calculation of the air gap flux-linkage of the 4-pole motor system, calculation and compensation of the unilateral magnetic pull, and decoupling calculation and induction compensation of the effective suspension control currents.

Figure 4 shows the flow chart of the ADC interrupt service program.

Next, several important program modules and the algorithm of the ADC interrupt service program are analyzed in detail. However, due to their complexity, other interrupt service programs, such as the outer interrupt service program, are not introduced here.

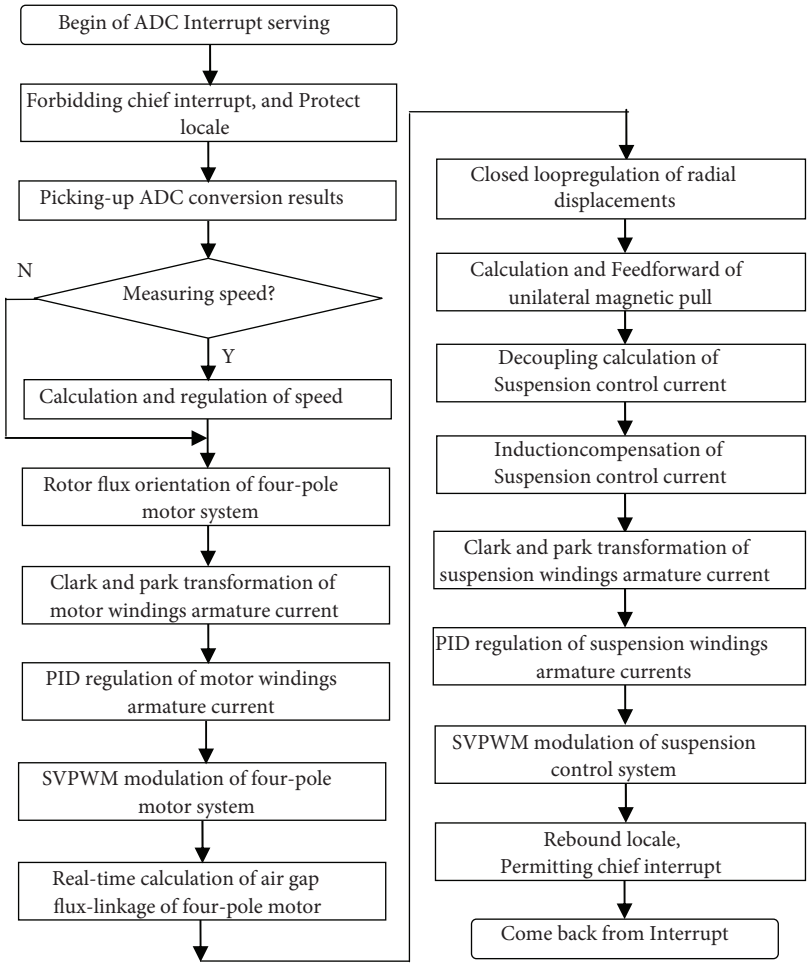

Figure 4. Flow chart of the ADC interrupt service program.

3.2. Calculation and regulation of rotational speed

To attain high performance from the rotational speed control, apart from the appropriate regulator, it is necessary to get an accurate speed in real time.

Here, an increment type encoder with 1024 lines is adopted. Whenever the rotor rotates in a circle in a mechanical space, the encoder emits A and B, i.e. double routes of the electric pulses, and the number of electric pulses in each route is 1024. The phase difference between the double routes of the signals is $\pi/2$ electric radians. According to the phase relationship between the double routes of the signals, the rotational direction of the motor is measured.

The double routes of the electric pulses are sent to the QEP encoding circuit of the DSP. By detecting the edge of each electric pulse, 4096 pulse signals are produced whenever the rotor rotates in a circle in the mechanical space. Next, the measurement error of rotor angle position is kept within 0.1 mechanical degrees, and then the rotational speed is expressed as in the following equation:

$$n = \frac{0.0146487375 \times PNB}{T_{speed}} \tag{2}$$

In Eq. (2), T_{speed} denotes the measurement period of the rotational speed, in seconds; PNB is the accumulative

total of the encoding pulses within a single T_{speed}; n is the rotational speed, in r/min.

Here, T_{speed} is set as 0.01 s, and then the rotational speed is expressed as in the following equation:

$$n = 1.46487375 \times PNB. \tag{3}$$

The reference signal n^* of the rotational speed is compared with n, and with regulation from the PID controller, the reference signal of electromagnetic torque is derived.

3.3. Correction and regulation of the measured displacements

There possibly exists an angle difference between the $\alpha\beta$ stationary reference frame and the installation position of the radial displacement sensors; the positions of 2 radial displacement sensors may not have a perpendicular relationship, as shown in Figure 5. If there are no correction measures, there may be coupling between the 2 components of the produced magnetic suspension force [8].

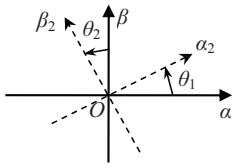

Figure 5. Installation reference frame of the radial displacement sensor.

In Figure 5, α_2 and β_2 denote the actual installation positions of the 2 radial displacement sensors. Next, the transformation relationship between the measured displacements and those in the $\alpha\beta$ reference frame can be expressed as in Eq. (4).

$$\begin{bmatrix} \alpha \\ \beta \end{bmatrix} = \begin{bmatrix} \cos\theta_1 & -\sin\theta_2 \\ \sin\theta_1 & \cos\theta_2 \end{bmatrix} \begin{bmatrix} \alpha_2 \\ \beta_2 \end{bmatrix} \tag{4}$$

To achieve reliable control of the radial displacements, it is necessary to constitute a closed-loop system for the radial displacements, i.e. by comparing the actual radial displacements with their reference signals, and by PID regulation, we then get the reference signals of magnetic suspension forces in directions α and β.

Now, the PID regulator is widely used in industrial control; the characteristics of its algorithm include being steady, reliable, and robust. Using a proportional regulator, the amplificatory multiple of an open loop can be changed, and the responding speed can be regulated; using an integral regulator, none of the static error of radial displacements can be achieved during steady operation; and using a differential regulator, the unreliable pole can be compensated for, and the dynamic stability of the system can be improved. However, the differential tache may magnify the unavoidable electromagnetic noise.

The improved PID regulator is adopted in the decoupling control of the radial displacement, i.e. a lowpass filter is adopted for the differential tache to depress the gain in the high frequency segment, and to reject the influence of high frequency noise. The adopted PID regulator of the radial displacements is shown in Figure 6.

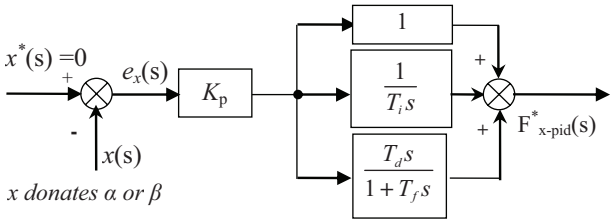

Figure 6. PID controller of the radial displacement.

3.4. Decoupling algorithm of the suspension control current

Models of the magnetic suspension force based on the parameters of a 2-phase bearingless motor were reported in [7–9]. However, the decoupling control model based on the parameters of a 3-phase bearingless motor should be more convenient for actual application.

MT is defined as the synchronous reference frame oriented by the air gap flux-linkage of the 4-pole motor; and DQ is defined as the synchronous reference frame oriented by the rotor flux-linkage of the 4-pole motor.

Next, from the theory analyses and mathematical derivation, the controllable magnetic suspension force of the 3-phase bearingless induction motor can be expressed as in Eq. (5).

$$\begin{bmatrix} F_\alpha \\ F_\beta \end{bmatrix} = K_m \begin{bmatrix} \psi_{4m} & 0 \\ 0 & -\psi_{4m} \end{bmatrix} \begin{bmatrix} i_{2m} \\ i_{2t} \end{bmatrix} \tag{5}$$

From Eq. (5), it can be derived that:

$$\begin{bmatrix} i_{2m} \\ i_{2t} \end{bmatrix} = \frac{1}{K_i} \begin{bmatrix} 1 & 0 \\ 0 & -1 \end{bmatrix} \begin{bmatrix} F_\alpha \\ F_\beta \end{bmatrix}. \tag{6}$$

In Eqs. (5) and (6), K_m is a configuration constant of the bearingless induction motor and K_i is the ratio parameter of the controllable magnetic suspension force to the effective suspension control current, in N/A. The 2 parameters can be expressed as in Eq. (7).

$$\left.\begin{array}{l} K_m = \frac{\pi L_{2ms}}{4\mu_0 RlN_{4i}N_{2i}} \\ K_i = K_m\psi_{4m} = \frac{\pi L_{2ms}\psi_{4m}}{4\mu_0 RlN_{4i}N_{2i}} \end{array}\right\} \tag{7}$$

In Eq. (7),

1) N_{2i} is the per-phase number of turns in a series of 3-phase 2-pole concentrated full-pitch suspension windings and N_{4i} is the per-phase number of turns in a series of 3-phase 4-pole concentrated full-pitch motor windings;

2) L_{2ms} is the per-phase magnetizing inductance of the 3-phase symmetry suspension windings;

3) ψ_{4m} is the air gap flux-linkage amplitude of the 4-pole motor in the synchronous reference frame.

To get better torque control performance, the rotor flux orientation strategy of the 4-pole motor is adopted. However, to facilitate the decoupling control of 2-pole magnetic suspension systems, the air gap flux information of the 4-pole motor is necessary. According to the vector control principle of the induction motor, the deviation angle $\Delta\theta$ of the air gap flux-linkage vector from the rotor flux-linkage vector, and the amplitude ψ_{4m} of the air gap flux-linkage, can be expressed as in Eq. (8).

$$\left.\begin{array}{l} \Delta\theta = \arctan\left\{L_{rl}i_{sq}/(\psi_r + L_{rl}i_{sd})\right\} \\ \psi_m = \sqrt{(\psi_r + L_{rl}i_{sd})^2 + (L_{rl}i_{sq})^2} \times L_m/L_r \end{array}\right\} \tag{8}$$

3.5. Compensation algorithm of the suspension control current

Aiming for a bearingless 4-pole induction motor with a pole-specific rotor, the authors in [12] and [13] presented methods to overcome the influence of the torque current component of the 4-pole motor, so as to avoid coupling between the 2 produced magnetic suspension force components. The authors in [12] presented a phase lead compensation method for the stator current vector of a 4-pole motor. In [13], the air gap flux orientation

strategy of a 4-pole motor was adopted to guarantee the accuracy of the air gap flux phase angle; however, the air gap flux orientation strategy of the 4-pole motor will lead to nonlinearity of the mechanical characteristics. If the rotor is pole-specific, then the rotor induction of the 2-pole magnetic suspension system can be neglected.

If the rotor windings are not pole-specific, the suspension magnetic field also inducts a current in the rotor windings [14], which influences the decoupling control performance of the bearingless induction motor. Aiming for a bearingless 2-pole induction motor where the rotor windings were not pole-specific, the authors in [15] presented the novel induction compensation method of a 4-pole magnetic suspension system by way of inverse function. However, no research aiming at a bearingless 4-pole induction motor, whose rotor windings are not pole-specific, with the rotor induction problem and its compensation method of a 2-pole magnetic suspension system have been reported.

It is known that the rotor's radial displacement is much smaller than the average air gap of a motor during steady operation; hence, in the single-phase equivalent circuit of a 2-pole magnetic suspension system, the mutual-inductance between the motor windings and suspension windings, caused by the slender rotor radial shift, can be neglected, and the transfer function from the armature current i_{2s} to the effective suspension control current i_{2m} can be expressed as in Eq. (9).

$$G(s) = \frac{I_{2m}(s)}{I_{2s}(s)} = \frac{r_2^{'}/s_2 + sl_{2\sigma}^{'}}{r_{2m} + sL_{2m} + r_2^{'}/s_2 + sl_{2\sigma}^{'}} \tag{9}$$

The rotational speed of a bearingless motor is mainly decided by the synchronous rotational speed of the 4-pole motor. For a 2-pole magnetic suspension system, the slip is approximately 0.5, i.e. '$s_2 \approx 0.5$'.

From the analyses of the logarithm frequency characteristics, it is known that, comparing with the armature current i_{2s} of the suspension windings, the effective control current i_{2m} is not only reduced in amplitude, but is also lagged in the phase angle.

Supposing that:

1) i_{2sm} and i_{2st} are the armature current components of the suspension windings along the M and T reference frame axes.

2) i_{2m} and i_{2t} are the effective suspension control current components along the M and T reference frame axes.

The relationship between the effective suspension control current $i_{2m,t}$ and the armature current $i_{2sm,t}$ of the suspension windings can then be expressed as in Eq. (10).

$$\begin{bmatrix} i_{2m} \\ i_{2t} \end{bmatrix} = \frac{1}{K_{rc}} \begin{bmatrix} \cos\theta_{rc} & \sin\theta_{rc} \\ -\sin\theta_{rc} & \cos\theta_{rc} \end{bmatrix} \begin{bmatrix} i_{2sm} \\ i_{2st} \end{bmatrix} \tag{10}$$

Here, K_{rc} is the amplitude ratio of the armature current vector to the effective control current vector and θ_{rc} is the lagged electric angle of the effective control current vector relative to the actual armature current vector.

If the compensation method is not adopted, i.e. if the armature current of the suspension windings is regarded as the effective suspension control current, then the rotor's induction current will result in a coupling between the 2 components of the produced magnetic suspension force. Here, the leading compensation is adopted and the compensation function can be expressed as in Eq. (11).

$$G_c(j\omega) = \frac{I_{2s}(j\omega)}{I_{2m}(j\omega)} = K_{rc}\angle\theta_{rc} \tag{11}$$

Here, K_{rc} and θ_{rc} can be expressed, respectively, as:

$$\left.\begin{array}{l} K_{rc}=\sqrt{\frac{(r_{2m}+r_2^{'}/s_2)^2+\omega^2(L_{2m}+l_{2\sigma}^{'})^2}{(r_2^{'}/s_2)^2+\omega^2(l_{2\sigma}^{'})^2}} \\ \theta_{rc}=arctg(\frac{\omega A}{1+\omega^2 B}) \end{array}\right\}. \tag{12}$$

In Eq. (12):

$$A=\frac{L_{2m}+l_{2\sigma}^{'}}{r_{2m}+r_2^{'}/s_2}-\frac{s_2 l_{2\sigma}^{'}}{r_2^{'}}, B=\frac{L_{2m}+l_{2\sigma}^{'}}{r_{2m}+r_2^{'}/s_2}\times\frac{s_2 l_{2\sigma}^{'}}{r_2^{'}}. \tag{13}$$

After compensation, the references of the suspension control current are converted to the armature current references of the suspension windings, as shown in Eq. (14).

$$\left[\begin{array}{c} i_{2sm}^{*} \\ i_{2st}^{*} \end{array}\right]=K_{rc}\left[\begin{array}{cc} cos(\theta_{rc}) & -sin(\theta_{rc}) \\ sin(\theta_{rc}) & cos(\theta_{rc}) \end{array}\right]\left[\begin{array}{c} i_{2m}^{*} \\ i_{2t}^{*} \end{array}\right] \tag{14}$$

In Eq. (14), i_{2m}^{*} and i_{2t}^{*} are the effective suspension control current references, which should be derived from the magnetic suspension decoupling controller, and i_{2sm}^{*} and i_{2st}^{*} are the armature current references of the suspension windings.

3.6. Compensation algorithm of the unilateral magnetic pulls

By parsing the inner Maxwell force, the precise model of the unilateral magnetic pull of the 3-phase bearingless induction motor in directions α and β can be derived as follows:

$$\left.\begin{array}{l} F_{\alpha-sm}=\frac{\pi l r B_{4m}^2}{2\mu_0\delta_0}\alpha+\frac{\pi l r B_{2m}^2}{4\mu_0\delta_0}\alpha(1-\frac{\varepsilon^2}{4}) \\ F_{\beta-sm}=\frac{\pi l r B_{4m}^2}{2\mu_0\delta_0}\beta+\frac{\pi l r B_{2m}^2}{4\mu_0\delta_0}\beta(1-\frac{\varepsilon^2}{4}) \end{array}\right\}. \tag{15}$$

In Eq. (15) B_{2m} is the amplitude of the air gap magnetic flux density of the 2-pole magnetic suspension system and B_{4m} is the same as that in Eq. (7).

The unilateral magnetic pull includes 2 parts, respectively, produced by the magnetic field of the 4-pole motor, and by the 2-pole suspension magnetic field. In usual operation, unless the radial load is too big, B_{2m} is far smaller than B_{4m}. The unilateral magnetic pull caused by the 2-pole suspension magnetic field can then be neglected. Next, there are the following approximate equations:

$$F_{\alpha-sm}\approx\frac{\pi l r B_{4m}^2}{2\mu_0\delta_0}\alpha, \quad F_{\beta-sm}\approx\frac{\pi l r B_{4m}^2}{2\mu_0\delta_0}\beta. \tag{16}$$

From the theory analyses, the air gap magnetic flux density of the 4-pole motor can be expressed as in Eq. (17).

$$B_{4m}=\sqrt{\frac{2}{3}}\frac{\psi_{4m}}{RlN_{4i}} \tag{17}$$

By putting Eq. (17) into Eq. (16) we get:

$$F_{\alpha-sm}\approx K_x\alpha, \quad F_{\beta-sm}\approx K_x\beta. \tag{18}$$

Here, K_x is the ratio parameter of the unilateral magnetic pull to the radial displacement of the 3-phase bearingless induction motor, in N/m. K_x can be expressed as in Eq. (19).

$$K_x = \frac{\pi \psi_{4m}^2}{3\mu_0 r l N_{4i}^2 \delta_0} \tag{19}$$

In Eqs. (18) and (19), N_{4i} and ψ_{4m} are the same as those in Eq. (7).

According to Eq. (18), the compensation signals of the unilateral magnetic pulls in directions α and β can be calculated online. By adding compensation signals on the reference signals of the controllable magnetic suspension force that is derived from the PID regulators, the feedforward compensation of the unsteady unilateral magnetic pull is achieved, as shown in Figure 7.

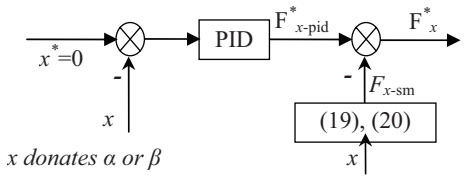

Figure 7. Feedforward compensation of the unilateral magnetic pull.

3.7. Current regulation and SVPWM modulation algorithm of the 2-pole magnetic suspension control system

By comparing the armature current reference and the actual armature current of suspension windings, and using the PID regulator, the reference signals of the armature voltages in the MT reference frame are derived. Next, by reverse revolving the transformation of the coordinates, the armature voltage references, i.e. u_α^* and u_β^*, are derived. u_α^* and u_β^* are then used in the SVPWM modulation.

Here, the adopted algorithm of the SVPWM modulation of the 2-pole suspension control system is introduced; the detailed approach is summarized in the following steps:

3.7.1. Confirming the sector index of the reference voltage vector

Figure 8 shows the distributing chart of the basic voltage vectors. To get the desired voltage vector, it is necessary to confirm which sector the desired voltage vector is located in.

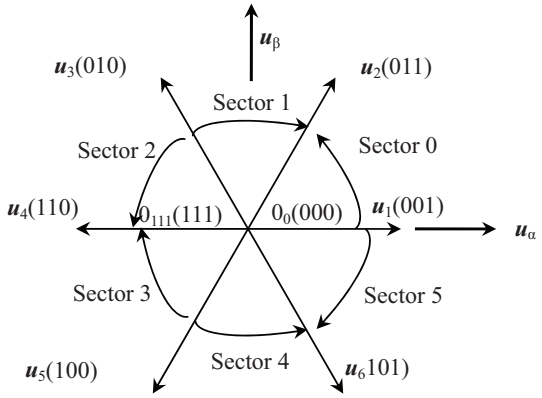

Figure 8. Sector chart divided by the basal space voltage vector.

Here, u_α^* and u_β^* denote the desired voltage vector. Next, several reference voltages are set in Eq. (20).

$$u_{r1} = u_\beta^*, u_{r2} = \frac{\sqrt{3}}{2}u_\alpha^* - \frac{1}{2}u_\beta^*, u_{r3} = -\frac{\sqrt{3}}{2}u_\alpha^* - \frac{1}{2}u_\beta^* \tag{20}$$

Variables C, D, and E are defined as following expressions:

$$C = \begin{cases} 1, u_{r1} > 0 \\ 0, u_{r1} < 0 \end{cases}, D = \begin{cases} 1, u_{r2} > 0 \\ 0, u_{r2} < 0 \end{cases}, E = \begin{cases} 1, u_{r3} > 0 \\ 0, u_{r3} < 0 \end{cases}. \tag{21}$$

Next, the sector index of the desired voltage vector can be calculated as in Eq. (22).

$$\sec index = C + 2D + 4E \tag{22}$$

3.7.2. Acquiring the action time per unit of the relevant basal voltage vectors

The corresponding relationship between the secindex values, the serial number of the sector where the desired voltage vector is located, and the action time per unit of the relevant basal voltage vectors, i.e. t_{1pu} and t_{2pu}, is summarized in Table 1.

Table 1. Action time per unit of the relevant basal voltage vector.

Secindex	Sector	t_{1pu}	t_{2pu}
1	1	-u_{r2}	-u_{r3}
2	5	-u_{r3}	-u_{r1}
3	0	u_{r2}	u_{r1}
4	3	-u_{r1}	-u_{r2}
5	2	u_{r1}	u_{r3}
6	4	u_{r3}	u_{r2}

Table 2 gives the corresponding relationship between the action time and the basal voltage vector. For example, when the desired voltage vector is located in sector 2, the action time per unit of the basal voltage vector u_3 corresponds to t_{1pu}, and that of the basal voltage vector u_4 corresponds to t_{2pu}.

Table 2. Corresponding relationship between the action time and basal voltage vector.

Action time / Sector	t_{1pu}	t_{2pu}
0	u_1	u_2
1	u_3	u_2
2	u_3	u_4
3	u_5	u_4
4	u_5	u_6
5	u_1	u_6

3.7.3. Given values of the 3 full comparing registers of EVA

T_{prd} is defined as the value of the register period. Next, the actual action time of the relevant basal voltage vector is calculated as in Eq. (23):

$$t_1 = t_{1pu}T_{prd}, t_2 = t_{2pu}T_{prd}. \tag{23}$$

If the sum of t_1 and t_2 is more than T_{prd}, then:

$$t_1 = t_1 \times \frac{T_{prd}}{t_1 + t_2}, t_2 = t_2 \times \frac{T_{prd}}{t_1 + t_2}. \tag{24}$$

In T_{prd}, the other time is the action time of the zero vectors, and can be divided into 2 parts, as in Eq. (25).

$$t_0 = \frac{T_{prd} - t_1 - t_2}{2} \tag{25}$$

Next, we adopt the transform relationship as in Eq. (26):

$$T_u = t_0, T_v = T_u + t_1, T_w = T_v + t_2. \tag{26}$$

Regardless of the sector, the 3 full comparing registers can be given values according to Table 3 and the desired SVPWM signals will be output from the PWM_1 – PWM_6 ports of the DSP COMS chip.

Table 3. Given values of the 3 full comparing registers.

Registers \ Sector	0	1	2	3	4	5
CMP1	T_u	T_v	T_w	T_w	T_v	T_u
CMP2	T_v	T_u	T_u	T_v	T_w	T_w
CMP3	T_w	T_w	T_v	T_u	T_u	T_v

3.8. Current regulation and SVPWM modulation algorithm of the 4-pole motor control system

The 3 full comparing registers of EVB are used to modulate the SVPWM signals of the 4-pole motor system. The current regulation and SVPWM modulation algorithms are the same as those of the 2-pole suspension control system. However, the SVPWM signals are output from the PWM_7 – PWM_{12} ports of the DSP CMOS chip, as shown in Figure 2.

4. Experimental result and analyses

Aiming for a 3-phase bearingless prototype induction motor, digital control experimental equipment is developed, and a reliable suspension control experiment is made.

Figure 9 shows the designed hardware circuit of the digital control system. Figure 9a shows the digital control hardware circuit and Figure 9b shows the drive circuit based on the intelligent power module (IPM) module. There are 2 sets of 3-phase full-bridge insulated-gate bipolar transistors in the FSBB20CH60-IPM module, and they are used as power inverters for the 4-pole motor system and 2-pole magnetic suspension control system. The detailed implementation of hardware system was presented in [16], and will not be introduced here in detail.

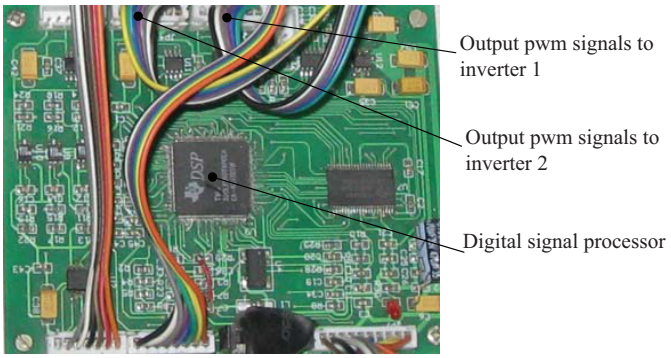

(a)

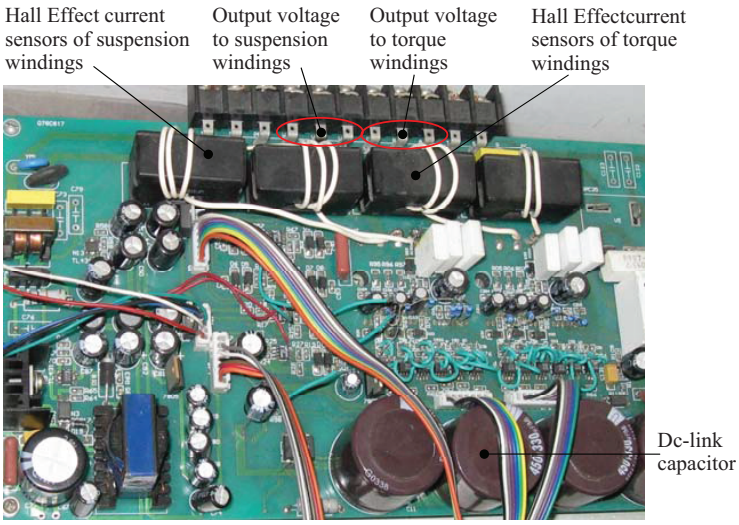

(b)

Figure 9. Digital control experimental equipment of the bearingless induction motor: a) photo of the digital control circuit based on DSP and b) photo of the drive circuit based on the IPM module.

Parameters of the 3-phase bearingless prototype induction motor:

1) Four-pole motor: 2.2 KW, $R_{1s} = 1.6\ \Omega$, $R_{1l} = 0.0043$ H, $R_{1r} = 1.423\ \Omega$, $L_{1rl} = 0.0043$ H, $L_{m1} = 0.0859$ H, J $= 0.024$ kg.m^2;

2) Two-pole magnetic suspension system: $R_{2s} = 2.7\ \Omega$, $L_{2l} = 0.00398$ H, $R_{2r} = 2.344\ \Omega$, $L_{2rl} = 0.00398$ H, $L_{m2} = 0.230$ H;

3) The average air gap length of the motor is 0.6 mm;

4) The average air gap length of the emergency mechanical bearing is 0.2 mm.

Figure 10 shows the radial displacement waves of the rotor in directions α and β during steady operation, with a radial load of about 100 N, and the radial load is in the reverse direction of the β reference frame axes.

Figure 11 shows the radial displacement waves of the rotor in directions α and β during acceleration. Before and after the acceleration, the motor operates reliably. In the course of acceleration, the radial displacements become a little bigger than those during steady operation, which is caused by a small fluctuation of the air gap flux-linkage of the 4-pole motor during acceleration.

In Figures 10 and 11, periodicity fluctuating characteristics are presented in the α and β radial displace-

ment waves, which are caused by the mass eccentricity of the mechanical rotor. The problem of the periodical vibrating of the bearingless motor and its control strategy will be discussed in future works.

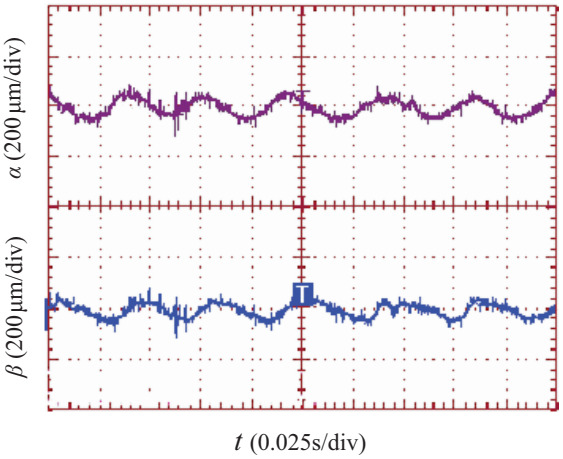

Figure 10. Radial displacement waves of α and β during steady operation.

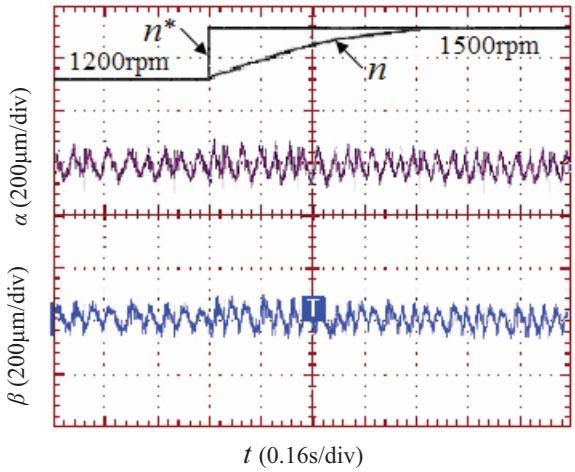

Figure 11. Radial displacement waves of α and β during acceleration.

5. Discussion and conclusions

The scheme and principle of the magnetic suspension decoupling control system of a 3-phase bearingless 4-pole induction motor with 2-pole suspension windings is presented, and the overall configuration of the digital control hardware system is introduced.

Next, based on the DSP CMOS chip, hardware equipment and decoupling digital control software are designed and implemented. In this paper, the calculation and regulation of the rotational speed, correction and regulation methods of the radial displacements, controllable magnetic suspension force model and compensation method of the unilateral magnetic pull applicable for a 3-phase bearingless induction motor, and SVPWM modulation algorithm are presented in detail. Moreover, aiming for the rotor induction problem of a 2-pole magnetic suspension system, the compensation algorithm of the effective suspension control current is analyzed and presented.

Finally, based on the designed digital control system of the 3-phase bearingless induction motor, the experimental results are presented and reliable suspension control is achieved. The experimental results verify the feasibility and practicability of the designed digital control system of the 3-phase bearingless induction motor. A minor defect in something otherwise perfect is that the periodical fluctuating characteristics are presented in α and β displacement waves, which is caused by the mass eccentricity of the mechanical rotor.

Regarding the periodical vibration problem, we will attempt to solve these 2 aspects in the near future. On the one hand, we will attempt to enhance the machining precision of the mechanical rotor, improve the install technics, and machine another bearingless prototype induction motor with higher precision. On the other hand, we will research the vibration principle and relevant control algorithm, and the vibration control system of the bearingless induction motor, so as to finally overcome the unbalance vibration problem of the bearingless induction motor. The problem of the periodical vibration of the 3-phase bearingless induction motor, and its control strategy, will be addressed in future works.

Acknowledgments

The support of National Natural Science Foundation of China (51277053), International Cooperation Project on Science and Technology of Henan Province (114300510029), and Nature Science Fund of Henan Province Education Bureau (2010B510011) is acknowledged.

Nomenclature

α	Radial displacement of the rotor in direction α.
β	Radial displacement of the rotor in direction β.
PNP	Accumulative total of the encoding pulses within a single measurement period of the rotational speed.
T_{speed}	Measurement period of the rotational speed.
n	Rotational speed in r/min.
$F_{sm\alpha}$	Unilateral magnetic pull in direction α.
$F_{sm\beta}$	Unilateral magnetic pull in direction β.
K_x	Ratio parameter of the unilateral magnetic pull to the radial displacement.
K_i	Ratio parameter of the controllable magnetic suspension force to the control current.
N_{4i}	Per-phase number of turns in the series of 3-phase 4-pole concentrated full-pitch motor windings.
N_{2i}	Per-phase number of turns in the series of 3-phase 2-pole concentrated full-pitch suspension windings.
L_{2ms}	Per-phase magnetizing inductance of the 3-phase symmetry suspension windings.
ψ_{4m}	Air gap flux-linkage amplitude of the 4-pole motor.
B_{4m}	Air gap magnetic flux density of the 4-pole motor.
K_{rc}	Amplitude ratio of the armature current vector to the control current vector.
θ_{rc}	Lagged electric angle of the control current vector relative to the armature current vector.

References

[1] J. Asama, R. Nakamura, H. Sugimoto, A. Chiba, "Evaluation of magnetic suspension performance in a multi-consequent-pole bearingless motor", IEEE Transactions on Magnetics, Vol. 47, pp. 4262–4265, 2011.

[2] H.I. Lee, S.Y. Yoo, "Toroidally-wound self-bearing BLDC motor with Lorentz force", IEEE Transactions on Magnetics, Vol. 46, pp. 2148–2151, 2010.

[3] H. Grabner, W. Amrhein, S. Silber, "Nonlinear feedback control of a bearingless brushless DC motor", IEEE/ASME Transactions on Mechatronics, Vol. 15, pp. 40–47, 2010.

[4] K. Raggl, B. Warberger, T. Nussbaumer, "Robust angle-sensorless control of a PMSM bearingless pump", IEEE Transactions on Industrial Electronics, Vol. 56, pp. 2076–2085, 2009.

[5] E.F. Rodriguez, J.A. Santisteban, "An improved control system for a split winding bearingless induction motor", IEEE Transactions on Industrial Electronics, Vol. 58, pp. 3401–3408, 2011.

[6] W.S. Bu, S.H. Huang, S.M. Wan, "General analytical models of inductance matrices of four-pole bearingless motors with two-pole controlling windings", IEEE Transactions on Magnetics, Vol. 45, pp. 3316–3321, 2009.

[7] S.R. Zhang, F.L. Luo, "Direct control of radial displacement for bearingless permanent-magnet-type synchronous motors", IEEE Transactions on Industrial Electronics, Vol. 56, pp. 542–552, 2009.

[8] H. Nian, Y.K. He, L. Huang, "Sensorless operation of an inset PM bearingless motor implemented by the combination approach of MRAS and HF signal injection", Proceedings of the World Congress on Intelligent Control and Automation, Vol. 2, pp. 8163–8167, 2006.

[9] X. Cao, Z.Q. Deng, G. Yang, "Independent control of average torque and radial force in bearingless switched-reluctance motors with hybrid excitations", IEEE Transactions on Power Electronics, Vol. 24, pp. 1376–1385, 2009.

[10] A. Chiba, J.A. Santisteban, "A PWM harmonics elimination method in simultaneous estimation of magnetic field and displacements in bearingless induction motors", IEEE Transactions on Industry Applications, Vol. 48, pp. 124–131, 2012.

[11] A. Chiba, K. Sotome, Y. Iiyama, "A novel middle-point-current-injection-type bearingless PM synchronous motor for vibration suppression", IEEE Transactions on Industry Applications, Vol. 47, pp. 1700–1706, 2011.

[12] A. Chiba, R. Furuichi, Y. Aikawa, "Stable operation of induction-type bearingless motors under loaded conditions", IEEE Transactions on Industry Applications, Vol. 33, pp. 919–924, 1997.

[13] T. Suzuki, A. Chiba, "An air-gap-flux-oriented vector controller for stable operation of bearingless induction motors", IEEE Transactions on Industry Applications, Vol. 36, pp. 1069–1076, 2000.

[14] T. Hiromi, T. Katou. A. Chiba, "A novel magnetic suspension-force compensation in bearingless induction-motor drive with squirrel-cage rotor", IEEE Transactions on Industry Applications, Vol. 43, pp. 66–76, 2007.

[15] W.S. Bu, J.Y. Xiao, L. Yuan, "Induction compensation control of bearingless induction motor", Proceedings of the IEEE ICMA, Vol. 1, pp. 944–949, 2011.

[16] W.S. Bu, S.C. Zhang, S.M. Wan, "Hardware implement of numerical control system for bearingless induction motor", Proceedings of the IEEE ICMA, Vol. 1, pp. 1934–1938, 2011.